Tungsten Trioxide and Its TiO$_2$ Mixed Composites for the Photocatalytic Degradation of NO$_x$ and Bacteria (*Escherichia coli*) Inactivation

Ermelinda Falletta [1] , Claudia Letizia Bianchi [1] , Franca Morazzoni [2,*], Alessandra Polissi [3] ,
Flavia Di Vincenzo [3] and Ignazio Renato Bellobono [4]

[1] Dipartimento di Chimica, Università degli Studi di Milano, Via Camillo Golgi 19, 20133 Milano, Italy;
ermelinda.falletta@unimi.it (E.F.); claudia.bianchi@unimi.it (C.L.B.)

[2] Dipartimento di Scienza dei Materiali, Università di Milano-Bicocca, Via Roberto Cozzi, 55,
20125 Milano, Italy

[3] Dipartimento di Scienze Farmacologiche e Biomolecolari, Università degli Studi di Milano,
Via Giuseppe Balzaretti, 9, 20133 Milan, Italy; alessandra.polissi@unimi.it (A.P.);
flavia.divincenzo@unimi.it (F.D.V.)

[4] Dipartimento di Fisica, Università degli Studi di Milano, Via Giovanni Celoria, 16, 20133 Milano, Italy;
i.r.bellobono@alice.it

[*] Correspondence: franca.morazzoni@unimib.it

Abstract: The increased air pollution and its impact on the environment and human health in several
countries have caused global concerns. Nitrogen oxides (NO$_2$ and NO) are principally emitted from
industrial activities that strongly contribute to poor air quality. Among bacteria emanated from the
fecal droppings of livestock, wildlife, and humans, *Escherichia coli* is the most abundant, and is often
associated with the health risk of water. TiO$_2$/WO$_3$ heterostructures represent emerging systems
for photocatalytic environmental remediation. However, the results reported in the literature are
conflicting, depending on several parameters. In this work, WO$_3$ and a series of TiO$_2$/WO$_3$ com-
posites were properly synthesized by an easy and fast method, abundantly characterized by several
techniques, and used for NO$_x$ degradation and *E. coli* inactivation under visible light irradiation.
We demonstrated that the photoactivity of TiO$_2$/WO$_3$ composites towards NO$_2$ degradation under
visible light is strongly related to the WO$_3$ content. The best performance was obtained by a WO$_3$
load of 20% that guarantees limited e$^-$/h$^+$ recombination. On the contrary, we showed that *E. coli*
could not be degraded under visible irradiation of the TiO$_2$/WO$_3$ composites.

Keywords: photocatalysts; visible light; tungsten trioxide; composites

1. Introduction

Due to growing industrialization, urban environments have faced chronic air pollution
issues in the last decades. Exhaust gases and burning fuels from factories represent the
primary sources of air pollutants on a global scale, causing a significant impact on human
health, animal and plant life, and climate [1]. Although natural sources responsible for air
pollutants production, such as broad forest fires, volcanic eruptions, and soil erosion, can
play a role in air pollution, the emissions resulting from human activities, such as motor
vehicle exhaust, combustion of fossil fuels, and industrial processes, are the most active
and concerning cause of air quality decline [2].

Nitrogen monoxide (NO) and nitrogen dioxide (NO$_2$), known as nitrogen oxides
(NO$_x$), are relevant pollutants whose emissions are directly related to human health prob-
lems [3], as they affect respiratory and immune systems [4], to the production of tropo-
spheric ozone, acid rains, and in general to global air pollution.

Over the years, different techniques have been developed for NO$_x$ abatement. Among
the traditional techniques, selective catalytic reduction (SCR) with ammonia in the presence

of oxygen is the most used, mainly applied to reduce NO_x emission from combustion processes [5], as well as absorption, adsorption, or electrical discharge processes [6]. However, all these methods are characterized by several limitations and disadvantages that make actual application hard. Moreover, the growing environmental constraints invoke restrictions regarding NO_x emission, requiring more efficient techniques for NO_x abatement.

In addition, awareness about the importance of supplying adequate drinking water has recently increased. In 2012, the United Nations estimated that nearly 11% of the world's population did not have access to improved drinking water sources. African water resources indeed contain high levels of microbial pathogens, including bacteria, viruses, and protozoa, as well as chemical contaminants. *Escherichia coli* and related bacteria constitute approximately 0.1% of gut flora, and fecal–oral transmission is the primary route through which pathogenic strains of the species cause disease. For that reason, new disinfection technologies are currently in development to fulfill the WHO Guidelines for drinking-water quality (World Health Organization, 2008). The traditional disinfection methods lead to chloro-organic disinfection by-products (DBPs) with carcinogenic and mutagenic effects.

In both study cases, using a TiO_2 semiconductor as a catalyst under UV or visible irradiation seems the most promising method.

Titania (TiO_2) has been considered the most efficient photocatalyst for a wide variety of applications, such as pollution abatement [7,8], water and air purification [9], antimicrobial applications [10], and energy conversion [11]. However, TiO_2 in its photoactive anatase phase has a wide band gap of 3.2 eV, limiting the photoactivity of the semiconductor only under UV irradiation [12]. Moreover, because of its suspected carcinogenic nature [13], researchers are willing to replace TiO_2 with new low-cost and visible-light-active smart materials.

Though many studies have focused on using TiO_2 [14–18], WO_3 and its composites have been poorly investigated to date [19–22].

WO_3 is a cheap, physiochemically stable, and mechanically robust semiconductor with a narrow band gap energy (2.4–2.8 eV), making it a visible-light-responsive photocatalyst for different applications [23–30]. Therefore, WO_3 represents a suitable choice for photocatalytic degradation under visible light irradiation.

As described in Figure 1, because the VB (valence band) edge potential of WO_3 is lower than that of TiO_2, upon photon absorption, electrons can be transferred from the conduction band of TiO_2 to WO_3, whereas photogenerated holes move in the opposite direction from electrons.
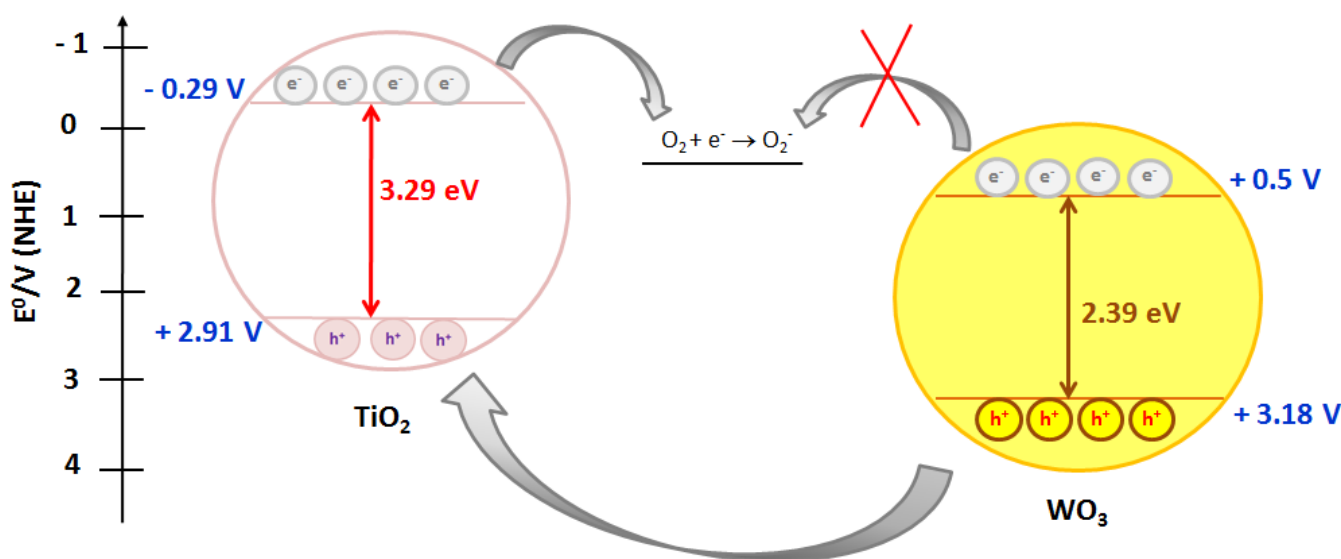

Figure 1. Photocatalytic mechanism of WO_3-loaded TiO_2 under light irradiation.

The transfer of photogenerated carriers is accompanied by consecutive W^{6+} reduction into W^{5+} by capturing photogenerated electrons at trapping sites in WO_3. In addition, W^{5+} ions on the surface of WO_3 are reoxidized into W^{6+}. However, the reduction potential value for the photogenerated electrons in the conduction band is not high enough for the single electron reduction in O_2 (Figure 1) [30]. The holes accumulated in the TiO_2 VB take part in the oxidation process to make OH^- or $OH^\cdot$ hydroxyl radical reactive species. These processes in WO_3/TiO_2 heterostructures restrain the recombination of electron–hole pairs significantly.

Different approaches have been developed to produce highly active TiO_2/WO_3 composites aiming to optimize the WO_3 content [31]. It has been demonstrated that the influence of WO_3 on TiO_2 photoactivity depends on several factors, such as crystal phase, electrons accumulation ability of WO_3, type of pollutants, and degradation pathways involved [31].

Yang et al. investigated the role of amorphous WO_x species, demonstrating that they are more active than the crystalline ones toward methylene blue degradation [32].

Other experiments by Žerjav et al. explained the correlation between the photocatalytic performance of TiO_2/WO_3 and their shallow and deep electron trapping states [33].

However, concerning WO_3 and its mixed oxides, the obtained results are conflicting because in the same cases, the presence of WO_3 seems to positively affect the photoactivity and the performances of TiO_2. In other cases, the results worsen [19,31,32,34].

Regarding NO_x degradation, Luévano-Hipólito et al. demonstrated that WO_3 with a polyhedral shape leads to 50% NO oxidation to NO_2 [19]. On the other hand, Yu and coworkers noticed for the first time the photo-transformation of NO_2 into NO in the presence of N_2 on the surface of a WO_3 photocatalyst under UV/visible light irradiation [20].

Recently, Mendoza et al. proposed TiO_2/WO_3 composites as efficient materials for NO_x abatement under visible light, leading to 90% of photodegradation in 1 h [22], whereas Paula and coworkers observed the decay of the photocatalytic activity of TiO_2/WO_3 heterostructures as a function of the W(VI) content [31].

Jawwad A. Darr et al. reported the easy disinfection of water by TiO_2/WO_3 mixed composites, which induce bacterial inactivation after 30 min of photo-irradiation [35].

In order to clarify the behavior of WO_3 and TiO_2/WO_3 heterostructures in the photocatalytic degradation of NO_x under visible light irradiation, in this work, WO_3 and a series of TiO_2/WO_3 composites were synthesized by a fast and cost-effective chemical procedure and tested for the photodegradation of NO_x and the inactivation of *E. coli* under visible light irradiation.

The role of the calcination temperature in the TiO_2/WO_3 preparation has been investigated and critically discussed, as well as the effect of the WO_3 loading in the final composites. Differently from the recent literature, the results proved that high calcination temperatures could cause complete or partial WO_3 sublimation with adverse effects on the activity of the TiO_2/WO_3 heterostructures.

Finally, while the synthesized catalysts were active in NO_2 photodegradation, they were inert to the antibacterial activity under visible light irradiation, in line with the scientific literature [36].

2. Results

2.1. Materials Characterization

Figure 2 shows the XRD patterns of all the synthesized materials.

TiO_2 exhibits the characteristics of diffraction peaks of anatase, as confirmed by the peaks at 25.3°, 37.7°, 48.0°, 53.8°, and 55.0°, with (101), (004), (200), (105), and (211) diffraction planes, respectively. The XRD pattern of WO_3 shows a crystalline phase characterized by diffraction peaks at 23.1°, 23.6°, 24.4°, and 34.2°, corresponding to the (002), (020), (200), and (202) crystal planes of monoclinic phase.
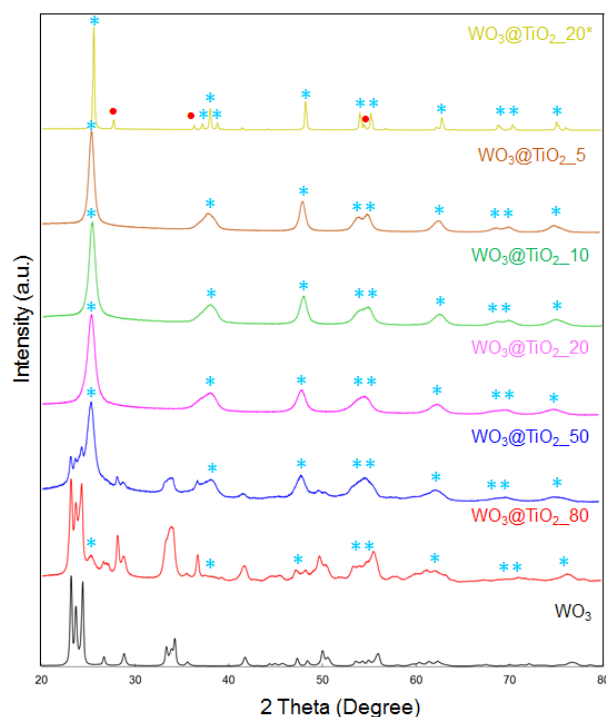
Figure 2. XRD patterns of the samples of Table 1 (* peaks of TiO_2 anatase, •peaks of TiO_2 rutile).

Table 1. Energy of band gap (eV), specific surface area, CBET, Vm, and mean pore diameter of the WO_3/TiO_2 composites series calcined at 400 °C. * Surface area by BET equation (2-parameters), ** mean pore diameter by BJH model from isotherm desorption branch ($0.3 < p/p0 < 0.95$).

Sample	Band Gap (eV)	* Specific Surface Area (m^2/g)	CBET	Vm (cm^3/g)	** Mean Pore Diameter (nm)
WO_3	2.39	4.00	75.75	0.94	21.17
$WO_3@TiO_2\_80$	2.63	42.78	123.22	9.92	8.6
$WO_3@TiO_2\_50$	3.05	110.65	98.11	25.87	6.4
$WO_3@TiO_2\_20$	3.14	179.78	75.50	43.26	6.0
$WO_3@TiO_2\_10$	3.26	139.47	94.7	33.15	6.8
$WO_3@TiO_2\_5$	3.20	111.08	112.87	31.29	9.1
TiO_2	3.29	318.00	84.48	75.50	4.70

As expected, in the $WO_3@TiO_2$ composites, the intensity of the diffraction peaks of WO_3 declines by decreasing the percentage of WO_3; on the contrary, anatase peaks intensity increases or appears with the higher concentration of TiO_2 in each composite.

Based on its XRD pattern, $WO_3@TiO_2\_20$* exhibits higher crystallinity degree if compared to the others and the appearance of new diffraction peaks can be observed.

As reported in the literature [37], it is directly correlated to the high temperature (600 °C) used for the calcination of this material. The degree of crystallinity increases with the temperature, and in the case of TiO_2-based compounds, at 600 °C the phase conversion from anatase to rutile starts.

According to the literature [22,34], when the WO_3 content in the composite materials is 20% or lower, the diffraction peaks of this semiconductor are undetected. Some authors justify this result with the presence of highly dispersed WO_3 small particles in TiO_2/WO_3 composites, which makes it hard to detect them by this technique [22,34]. In addition, Yang et al. demonstrated that when the loading amount of WO_3 was below 3 mol%, it exists in highly dispersed amorphous species that do not respond to XRPD. However, accurate

quantification of WO_3 loading on TiO_2 after calcination is necessary to verify unequivocally the WO_3/TiO_2 composite formation rather than a superficial W doping on the TiO_2 surface. In the present work, this was easily carried out by the reaction yield calculation (Equation (2)) and by EDS analysis (Table S1) for two composites with a nominal WO_3 load of 20% ($WO_3@TiO_2\_20$ and $WO_3@TiO_2\_20*$) calcined at two different temperatures (400 °C and 600 °C). From the results of the reaction yield, the $WO_3@TiO_2\_20*$ composite calcined at 600 °C exhibits a mass loss of approximately 40%, unlike the same sample calcined at 400 °C, obtained with a yield of 94.8%. Since WO_3 is a low-temperature sublimation material [38], it cannot be excluded that by increasing the calcination temperature, a complete or partial WO_3 sublimation can occur, as also confirmed by the EDS results (Table S1), where the measured percentage of WO_3 in the final composite is lower than 3%, whereas the material calcined at 400 °C shows a 27% of WO_3.

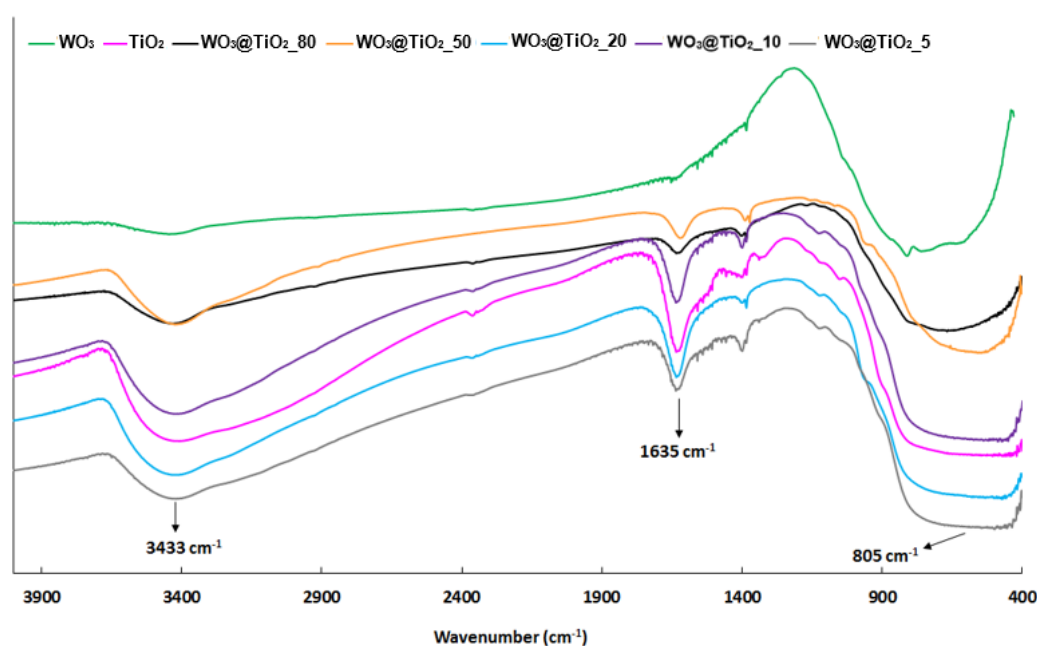Figure 3 displays the FT-IR for all the synthesized composites calcined at 400 °C.

Figure 3. FT−IR spectra of the samples calcined at 400 °C.

The FT-IR spectrum of WO_3 exhibits characteristic vibration bands, such as those at approximately 3433 cm^{-1} and 1635 cm^{-1}, that can be associated with the symmetric stretching vibrations of WO_3 and intercalated water molecules and the deformation vibrations of H–O–H bonds of the adsorbed water molecules, respectively, and the signal at 805 cm^{-1}, attributed to O–W–O stretching modes of WO_3 [39].

On the other hand, the FT-IR spectrum of TiO_2 nanoparticles is characterized by several peaks. The OH stretching mode of the hydroxyl groups is responsible for the broad band observed in the range of 3600–3000 cm^{-1}, indicating the presence of moisture in the sample. The band at approximately 1605 cm^{-1} is due to the OH bending vibrations of the absorbed water molecules. Finally, the broadband between 1000 and 500 cm^{-1} can be related to the Ti–O stretching and Ti–O–Ti bridging stretching modes [40].

As expected, in the FT-IR spectra of the composites, the WO_3 characteristic bands are covered by the more intense ones of TiO_2.

The optical properties of the synthesized WO_3/TiO_2 series calcined at 400 °C, as well as of single-phase semiconductors, were investigated by UV–Vis scanning spectrophotometry (Figure 4).

The main absorption edges of the samples are all around 400 nm, attributing to the excitation of electrons from the valence band to the conduction band. As reported in the literature [41], the empty orbitals of W^{6+} (W 5d) are closed to the Ti 3d orbitals of the

conduction band. Therefore, the $O_{2-} \rightarrow W^{6+}$ charge transfer transitions are overlapped with the $O_2 \rightarrow Ti^{4+}$ charge transfer transitions. Increasing the WO_3 loading, the absorption edge of photocatalysts red-shifts. If this is only slightly noticeable up to 10%, increasing the WO_3 percentage to 50% and above, the effect is much more evident, and the absorption edges of these materials are shifted at higher wavelengths.
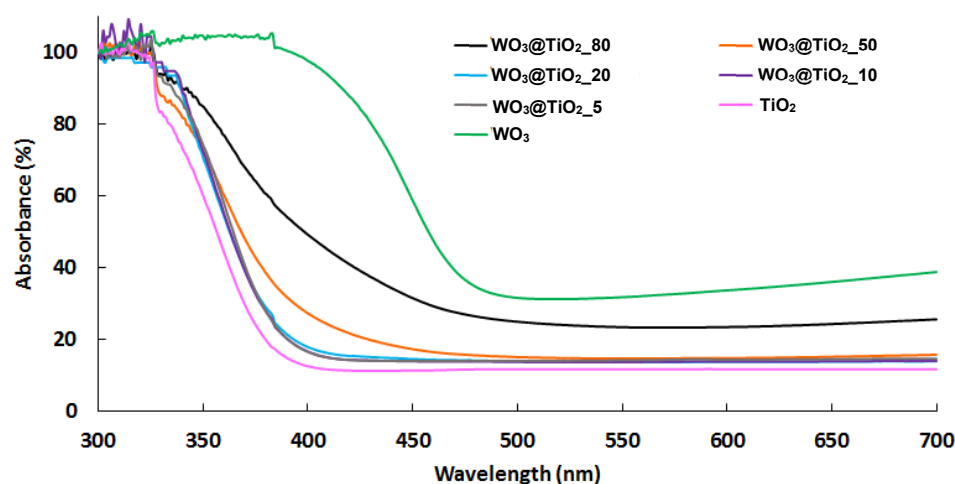

Figure 4. UV–Vis absorption spectra of the WO_3/TiO_2 composites series calcined at 400 °C.

The band gaps of the materials, estimated by the Kubelka–Munk function, are summarized in Table 1, and the Tauc plots are reported in Figure S2.

Samples Eg decreases, increasing the tungsten content, due to the formation of defective energy levels within the forbidden band gap of WO_3. On the other hand, by increasing the TiO_2 content, the total band gap of the photocatalyst decreases [42].

According to the shape of nitrogen adsorption–desorption isotherms reported in Figure 5 and the IUPAC classification [43], all the photocatalysts calcined at 400 °C can be classified as mesoporous materials of type IV, as confirmed by the values of C_{BET} in Table 1, containing other quantitative data.
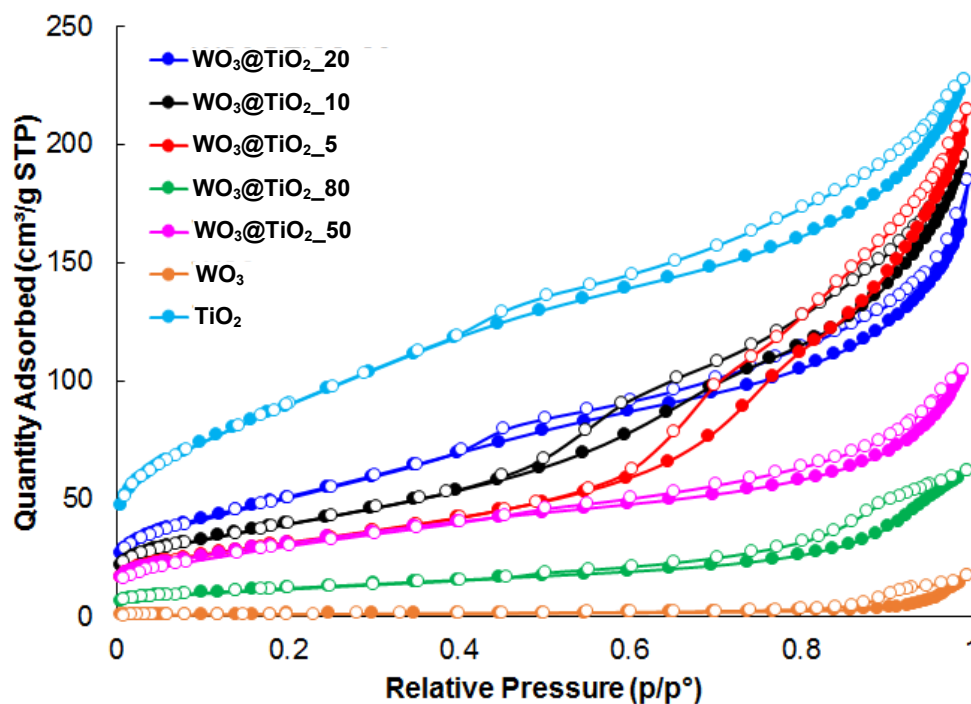

Figure 5. Nitrogen adsorption–desorption isotherms for the synthesized samples.

Figure 6 displays the SEM images and the elemental mapping of Ti and W for the synthesized composites, whereas the EDX spectra are reported in the (Supplementary Information Table S1).
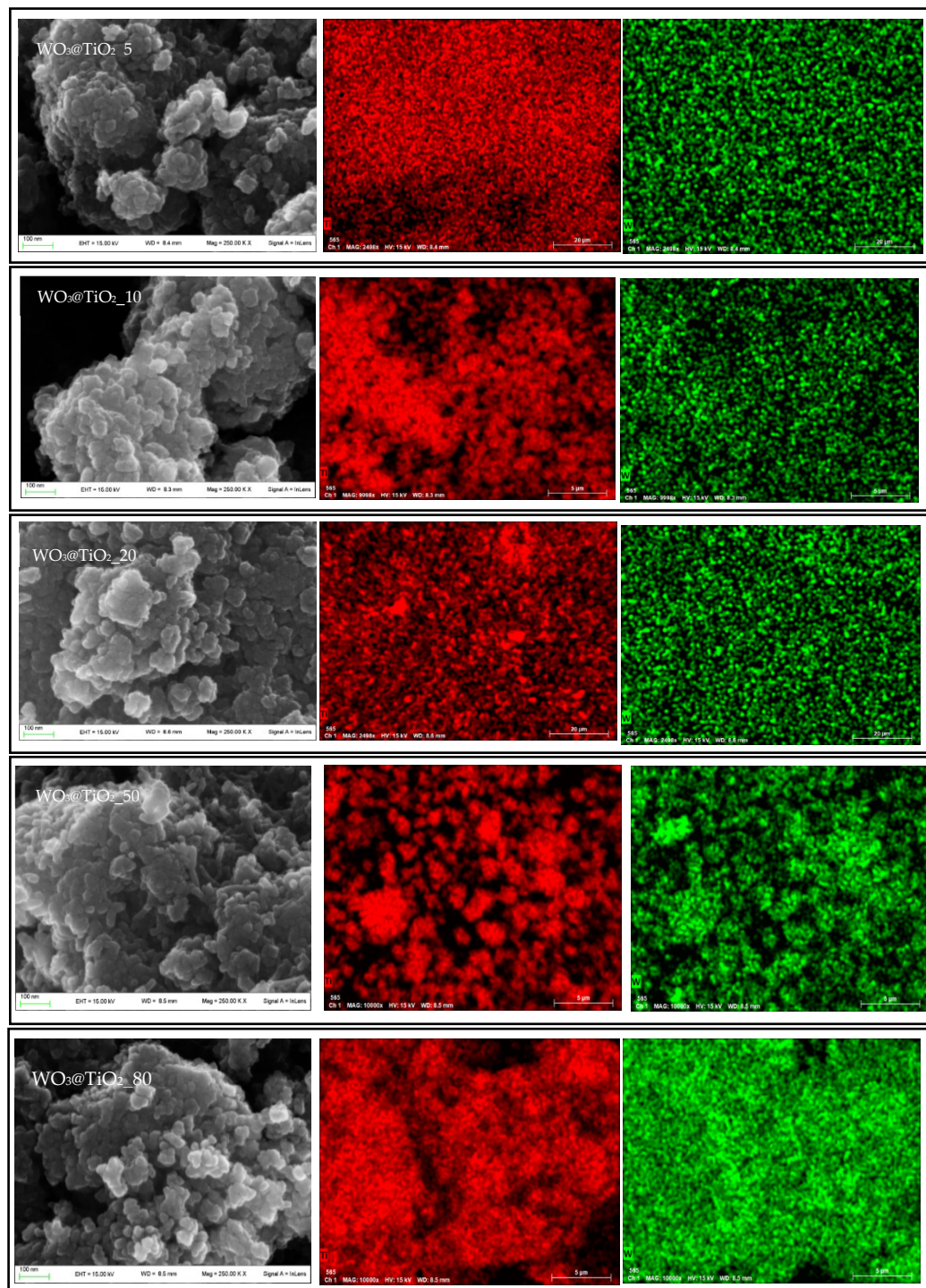
Figure 6. SEM images and elemental mapping of the synthesized materials. (**left**) sample analyzed, ((**middle**), red-colored) titanium map, ((**right**), green-colored) tungsten map.

The elemental maps of W and Ti by X-ray energy dispersion (EDX) in the composites demonstrate that TiO_2 and WO_3 are well dispersed in each material. All the $WO_3@TiO_2$ show a globular-like morphology with particle sizes ranging from 60 to 5 nm. The particles are aggregated by sharing corners or edges that probably involve the formation of Ti–O–W

bonds [44]. The same information was obtained by TEM investigations (Figure 7) showing nanoparticles of 12–35 nm that gradually aggregate with the WO_3 load, reaching up to 60 nm in size.
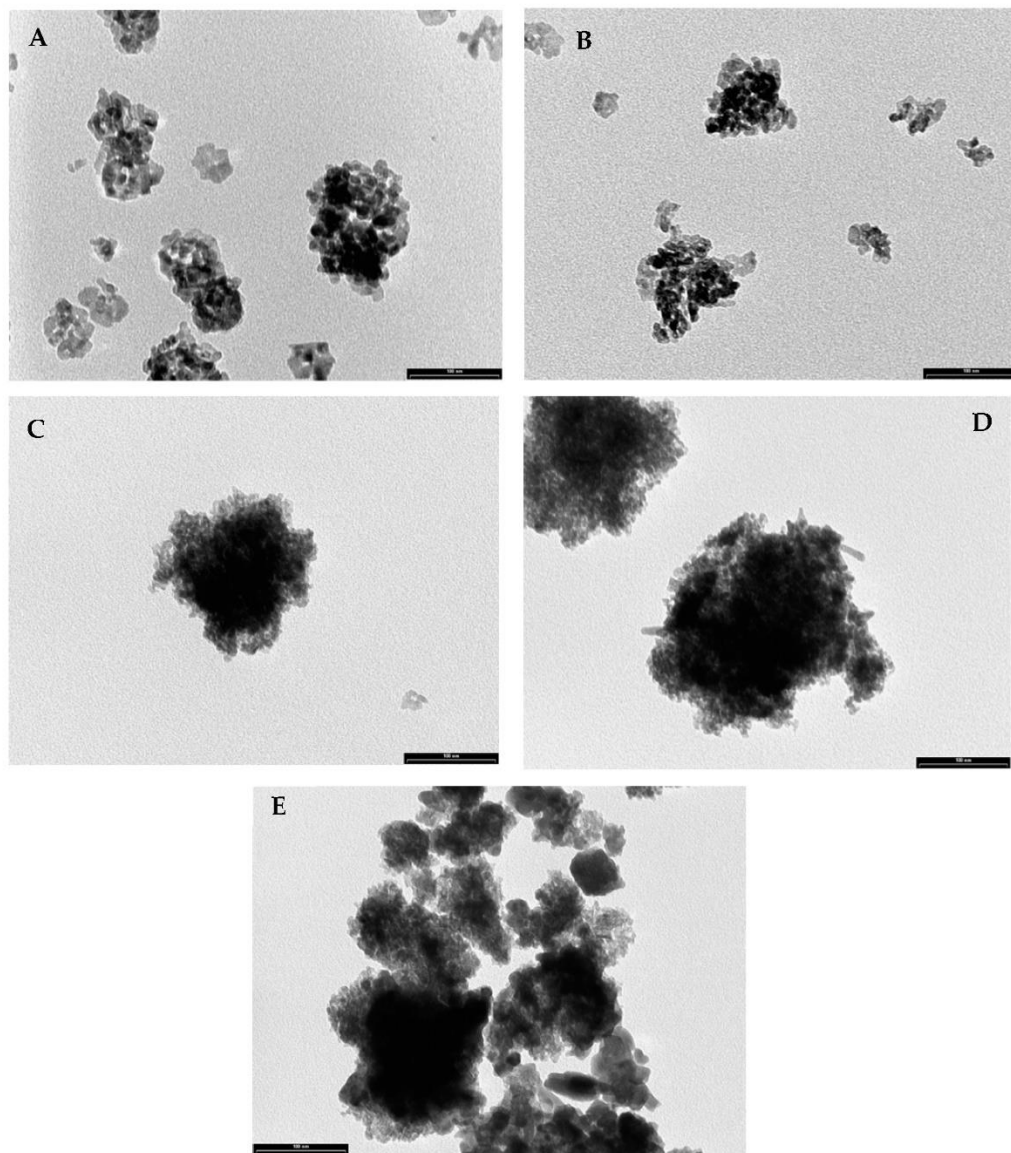
Figure 7. TEM images of WO_3@TiO_2_5 (**A**), WO_3@TiO_2_10 (**B**), WO_3@TiO_2_20 (**C**), WO_3@TiO_2_50 (**D**), WO_3@TiO_2_80 (**E**).

2.2. Photocatalytic and Biological Activities of Catalysts

2.2.1. NO_x Photocatalytic Degradation

The photocatalytic activity of the TiO_2/WO_3 composites, as well as single-phase photocatalysts, referred to both NO_x (NO + NO_2) and NO_2 conversion under visible light irradiation (Figure 8).
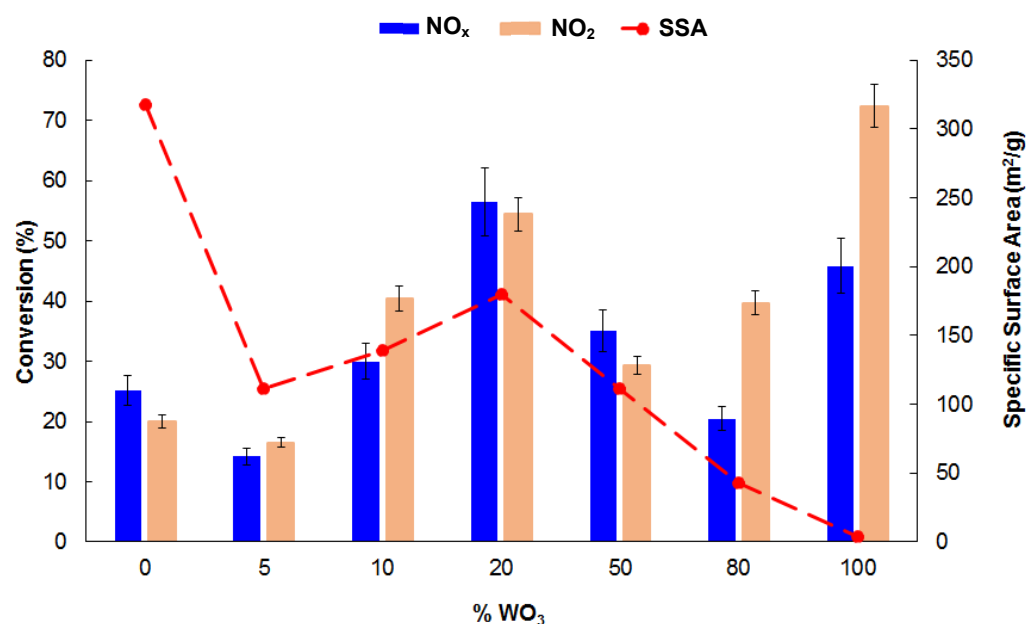
Figure 8. Dependence of NO_x and NO_2 photodegradation on WO_3 content and specific surface area (SSA) of the materials.

According to the literature [22,31,45], for this type of material the photocatalytic degradation of NO_x consists of a photo-oxidation process, where both NO and NO_2 species are first adsorbed on the surface of the heterostructures and then converted into the corresponding oxidation product (NO_3^-) under light irradiation. Although the formation of the oxidation products was well documented in the literature [46,47], an analytical confirmation was not performed in the present work due to the low NO_x concentrations used during the test.

For all the experiments, the initial concentration of NO_x was approximately 500 ppb. The NO_x photodegradation results are summarized in Figure 8.

As expected, despite its extraordinarily high surface area, TiO_2 shows poor activity towards NO_x conversion under visible light irradiation, leading to NO_x and NO_2 degradation in 25% and 20%, respectively. On the other hand, according to the band gap value, regardless of its low surface area, pristine WO_3 exhibits a good photoactivity towards NO_2 photodegradation (72%) in 3 h, whereas the NO_x abatement is only 46%. In fact, as reported in the scientific literature [19–22], WO_3 can remarkably reduce NO_2 into NO in the presence of N_2. This is confirmed by the results reported in Figure S3, showing for the WO_3 sample an increase in the NO concentration during the reaction. This makes pristine WO_3 not efficient in the NO_x abatement, because, as it is known, in air NO is immediately reoxidized to NO_2. In this regard, from the pioneering investigations of Yu et al., carried out under nitrogen atmosphere and UV irradiation, a 20% conversion of NO_2 into NO can be inferred [20]. The present results demonstrate that even under visible light irradiation, the percentage of NO formation from NO_2 is of the same order (24%), calculated by Equation (1):

$$NO \text{ produced } (\%) = \frac{[NOt] - [NOi]}{[NOt]} \tag{1}$$

where [NOt] is the NO concentration at the end of the reaction (after 3 h of light irradiation), [NOi] is the NO concentration before light irradiation.

If compared to the single-phase photocatalysts (TiO_2 and WO_3), the photoactivity of WO_3/TiO_2 heterostructures strongly depends on their composition. More in detail, the activity of the catalysts gradually increases with the WO_3 load, reaching the highest photodegradation efficiency by WO_3@TiO_2_20 (54.4% NO_x conversion and 56.4% NO_2

abatement), whereas it decreases for a percentage of WO_3 > 20. These results are in line with the pioneering investigations of Balayeva et al., who tested the photocatalytic activity of TiO_2/WO_3 composites towards NO degradation under UV irradiation, obtaining a ca. 35% of conversion for heterostructures characterized by a 1% and 2.5% of WO_3 load [48].

For a very high amount of WO_3 ($WO_3@TiO_2\_80$), these latter composites maintain the photoactive capability of pristine WO_3, converting NO_2 to NO. The different photoactivity of the materials may be due to a combination of factors.

First of all, it can be assumed that for a WO_3 load < 20%, TiO_2 and WO_3 only play their own photocatalytic role, and coupled photocatalysts are not formed. In this case, the low activity of TiO_2 prevails because it is the major component. In contrast, for a large amount of WO_3, the fast e^-/h^+ recombination of the WO_3 component predominates.

On the contrary, the absence of WO_3 peaks in the XRD spectra of the $WO_3@TiO_2\_20$ sample suggests that its increased photoactivity is not related to the formation of crystalline tungsten oxide but is probably due to the presence of WO_3 centers on the surface of TiO_2 acting as electrons/holes separators [49]. When the test was carried out using $WO_3@TiO_2\_20*$, in order to observe the effect of calcination temperature on the photoactivity of the material, the percentage of NO_x and NO_2 degradation dropped to ca. 20%, confirming that the thermal treatment acts by reducing the WO_3 content in the $WO_3@TiO_2$ heterostructure and as a consequence of its activity.

It is known that the quantum efficiency of photocatalytic reactions carried out by heterogeneous photocatalysts depends on the competition between the recombination of photogenerated electrons and holes and the transfer of both electrons and holes at the interface of the material. Extending the electrons and holes recombination time and increasing the transfer rate of electrons at the interface enhance the quantum efficiency positively. As reported in the literature [31], the formation of TiO_2/WO_3 heterostructures leads to enhanced charge carrier lifetimes, due to the transfer of photogenerated electrons in the TiO_2 to WO_3 CB, and at the same time to the entrapment of the photogenerated holes within the TiO_2 particle. Both these phenomena make charge separation more efficient.

Finally, the effect related to the different surface area values cannot be ignored. As for the photocatalytic activity, the surface area values also seem to be correlated to the WO_3 load and the most active catalyst ($WO_3@TiO_2\_20$) is also the one with the highest surface area (Figure 8, Table 1). At first glance, the results obtained by the $WO_3@TiO_2\_20$ photocatalyst seem to contrast with those of Mendoza et al. [22], who report very high NO conversion values under visible light irradiation in similar conditions. The different photocatalytic activity of the $WO_3@TiO_2\_20$ sample compared to those reported by Mendoza and coworkers can be reasonably attributed to the real WO_3 content in the synthesized composites that it is not specified in the work of the author [22].

2.2.2. *E. coli* Photoinactivation

The antibacterial activity of $WO_3@TiO_2$ composites, as well as single-phase photocatalysts, was assessed by determining the percentage of *E. coli* cell survival following exposure to visible light. According to standard methods (ASTM E2149, 2001), values of survival $\leq$ 90% indicate the antibacterial activity of a given photocatalytic film.

As shown in Figure 9, none of the tested samples displays antibacterial activity under visible light irradiation, in agreement with what was reported in the literature for the WO_3/TiO_2 catalyst [36].
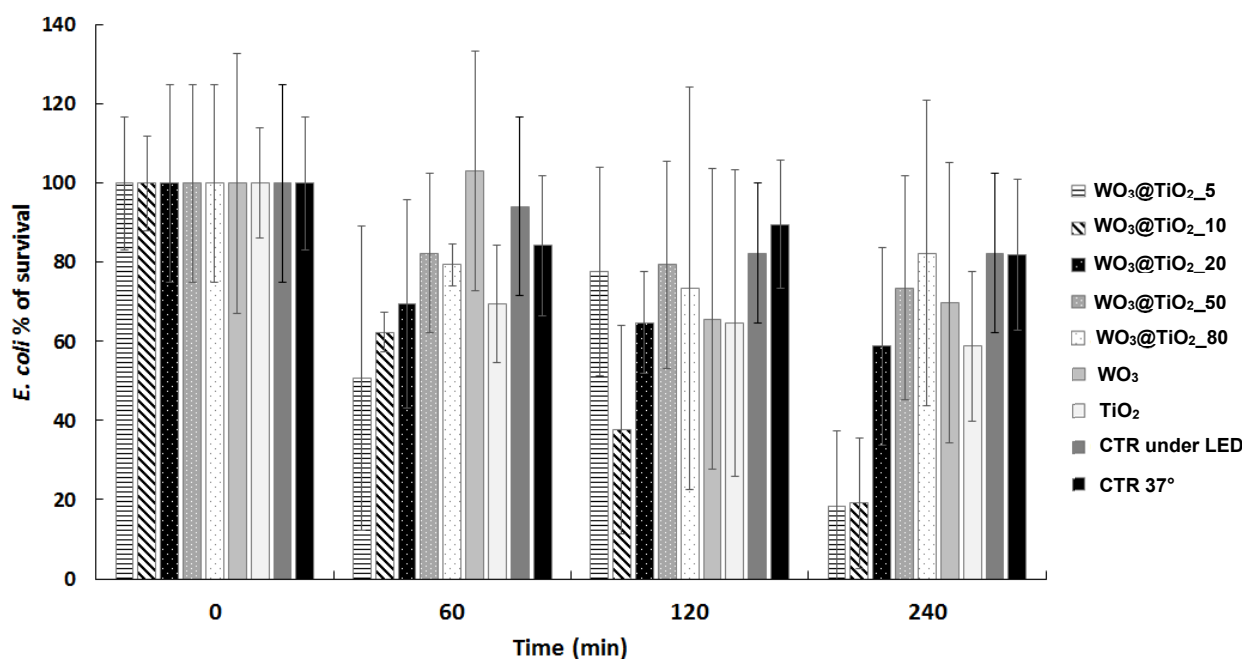
Figure 9. Percentage of *E. coli* cell survival after exposure to visible light in the presence of the synthesized heterostructures.

Different catalysts (e.g., sulfur-doped carbon quantum dots loaded hollow tubular g-C_3N_4) give degradation of *E. coli* cells instead, under visible light [50].

Based on the morphology of nanoparticles (Figure 7), we speculate that the nanoparticle aggregation of TiO_2/WO_3 hinders a suitable surficial interaction with the bacteria and the catalyst cytotoxicity.

3. Materials and Methods

3.1. Chemicals

Tungstic acid (H_2WO_4, 99% Merck), AMT 100 TiO_2 (Tayca Corporation, WP0097, Osaka, Japan), ammonium hydroxide solution (ACS reagent, 28.0–30.0% Merck & Co., St. Louis, MO, USA), hydrochloric acid (HCl 36%, Suprapur®, Supelco, Belfont, PA, USA) were used as received.

3.2. Synthesis of TiO$_2$/WO$_3$ Series

To synthesize 1 g of TiO_2/WO_3 composite, a proper amount of TiO_2 was dispersed in 25 mL of 2 M ammonium hydroxide solution under constant stirring (solution A). The WO_3 precursor solution was prepared by dissolving a proper amount of tungstic acid H_2WO_4 in 25 mL of 2 M ammonium hydroxide solution under constant stirring (solution B). The quantity of TiO_2 and H_2WO_4 used is reported in Table 2. The two solutions were stirred for 30 min at room temperature, then solution B was added to solution A and the stirring was continued for another 2 h at room temperature. Then, the solvent was evaporated, heating the mixture at 110 °C. The white-yellow powder was treated with 0.5 M hydrochloric acid solution and dried again. The final powder was washed with deionized water abundantly, dried at 100 °C overnight, and calcinated in the air at 400 °C for 2 h (heating rate 8 °C·min^{-1}). The synthesized samples containing different TiO_2/WO_3 *w/w* ratios (95:5, 90:10, 80:20, 20:80) were properly characterized and tested for NO_x photodegradation under visible light irradiation.

Table 2. Labels of the WO_3/TiO_2 composites, WO_3/TiO_2 w/w ratio, calcination temperature, and reaction yield.

Label	TiO$_2$ (g)	H$_2$WO$_4$ (g)	WO$_3$/TiO$_2$ (w/w Ratio)	Calcination Temperature (°C)	Yield (%)
WO$_3$	0.00	1.08	100:0	400	95.2
WO$_3$@TiO$_2$_80	0.20	0.86	80:20	400	95.7
WO$_3$@TiO$_2$_50	0.50	0.55	50:50	400	95.1
WO$_3$@TiO$_2$_20	0.80	0.22	20:80	400	94.8
WO$_3$@TiO$_2$_10	0.90	0.11	10:90	400	96.2
WO$_3$@TiO$_2$_5	0.95	0.05	5:95	400	95.7
WO$_3$@TiO$_2$_20*	0.80	0.22	20:80	600	60.9
TiO$_2$	1.00	0.00	0:100	400	98.5

WO_3 was synthesized by the same procedure using a TiO_2-free solution A.

An aliquot of the TiO_2/WO_3 composite with an 80:20 w/w ratio was calcined at 600 °C.

Table 2 reports a list of synthesized composites with the corresponding label, WO_3/TiO_2 w/w ratio, calcination temperature, and reaction yield, calculated by Equation (2):

$$\text{Yield } (\%) = \frac{\frac{g\ (H_2WO_4)\ \times\ molar\ mass(WO_3)}{molar\ mass\ (H_2WO_4)} + g\ TiO_2}{g\ final\ product} \tag{2}$$

3.3. Characterization Methods

X-Ray Diffraction (XRD) measurements investigated the crystalline structure on a PW3830/3020 X'Pert diffractometer (PANalytical, Almelo, The Netherlands) working Bragg–Brentano, using the Cu Kα1 radiation (k = 1.5406 Å).

FT-IR spectra were recorded in the range of 400–4000 cm^{-1} with a resolution of 0.5 cm^{-1} by anPerkin-Elmer spectrometer (Perkin Elmer, Waltham, MA, USA) dispersing a few milligrams of each material in anhydrous KBr. The morphology of the catalysts was inspected employing high-resolution electron transmission microscopy (HR-TEM), using a JEOL 3010-UHR instrument (Musashino Akishima, Japan; acceleration potential: 300 kV; LaB6 filament), and by scanning electron microscopy (SEM), using a Zeiss LEO 1525 field emission microscope (Jena, Germany). The samples were "dry" dispersed on lacey carbon Cu grids for TEM analyses, whereas SEM analyses were carried out without any pre-treatment of the samples.

For the band gap determinations, diffuse reflectance spectra of the powders were collected on a UV–Vis diffuse reflectance spectra using a scanning spectrophotometer PerkinElmer, Lambda 35 (Perkin Elmer, Waltham, MA, USA), which was equipped with a diffuse reflectance accessory. A thin film of each sample was placed in the sample holder on an integrated sphere for the reflectance measurements. A KBr pill was used as the reference material. Data were elaborated using the Kubelka–Munk function (Equation (3)), which expresses the adsorbance as a function of reflectance (F(R)) [51]:

$$F(R) = (1 - R)^2/2R \tag{3}$$

where R = reflectance of the powder.

The band gap values were determined by performing the first derivative of the Kubelka–Munk function (Equation (4)):

$$dF(R)/d\lambda \tag{4}$$

where λ = wavelength of the incident radiation. The energy of the radiation at which the first derivative dF(R)/d λ shows the maximum was taken to estimate the band gap values.

Specific surface area and porosity distribution were determined by processing N_2 adsorption–desorption isotherms at 77 K (Coulter SA3100 instrument, Beckman Life Sciences, Los Angeles, CA, USA) with Brunauer–Emmett–Teller (BET) and Barrett–Joyner–Halenda analyses. Before the analysis, samples were heat-treated (T = 150 °C, 4 h, N_2) to remove adsorbed foreign species.

3.4. NO_x Photodegradation Tests

A photocatalytic film of each sample was deposited by drop-casting on glass supports as follows: a suspension of 0.050 ± 0.001 g of photocatalyst in 5 mL of isopropanol was deposited on a glass plate (230×19 mm). Once the solvent was evaporated, the photocatalyst was placed inside a 20 L Pyrex glass cylindrical batch reactor for the photocatalytic tests. The photocatalytic tests were performed by a mixture of NO and NO_2 in air. The starting inlet gas contains only NO_2, but the chemical equilibrium between NO and NO_2 is established as it is exposed to air. An LED lamp (350 mA, 9–48 V DC, 16.8 W) with emissions in the 400–700 nm range was used as the light source. The luminous intensity (lux) was measured using an illumination meter (Delta Ohm photo/radiometer HD 2102.2) and was 2900 lx to estimate the light intensity. It was then converted to the irradiance unit (in mW/cm^2) [19], obtaining a light intensity of 3.24 mW/cm^2.

The NO_x initial concentration was 500 ± 50 ppb. A chemiluminescence analyzer measured the NO_x concentration after 30, 60, and 180 min of exposure to light irradiation (ENVEA AC32e).

3.5. Antibacterial Assay

Cultures of *E. coli* MG1655 [52] were grown at 37 °C in Luria–Bertani (LB) medium (10 g/L tryptone, 5 g/L yeast extract, 10 g/L NaCl) or LB-agar medium (LB medium with 10 g/L agar). Bacteria (200 mL) were collected by 10 min centrifugation at 5000 rpm, washed in PBS 1X (Merck & Co., St. Louis, MO, USA), and resuspended in the same volume of PBS 1X. Stationary phase cultures of *E. coli* were diluted up to optical density at 600 nm (OD600) of 0.05 and then grown aerated up to 0.6.

Films of the synthesized heterostructures were prepared as follows. A total of 100 mg of each material was dispersed in 8 mL of isopropanol and deposited on a Petri dish (90 mm in diameter) by drop-casting and air-dried.

10 mL of bacterial cells were added to Petri dishes. The plates were irradiated with visible light (2900 lux obtained with an LED lamp) and removed from light at different time points (60, 120, and 240 min). As controls, bacterial cells were deposited onto empty Petri dishes and irradiated (CTR under LED) or incubated at 37 °C under dark (CTR). Viable bacteria expressed as CFU/mL (colony-forming unit /mL) were enumerated at t = 0, 60, 120, and 240 min by plating suitable dilutions onto LB-agar plates following incubation at 37 °C for 18 h.

The percentage of bacterial survival is expressed as follows:

(average of viable bacteria at a given time/average of viable bacteria CTR 37° at t = 0 min) $\times$ 100.

The average of viable bacteria is calculated from at least three independent experiments. Values of survival $\leq$90% indicate the antibacterial activity of a given photocatalytic film.

4. Conclusions

In this study, we investigated the photoactivity of WO_3 and TiO_2/WO_3 composites towards NO_2 degradation under visible light, in order to clarify the numerous conflicting data reported in the literature so far. It was demonstrated that the photoactivity of TiO_2/WO_3 heterostructures are strongly related to their composition. For $WO_3@TiO_2$ materials characterized by low tungsten trioxide content (<20%), TiO_2 and WO_3 are present as separate phases, each playing their own photocatalytic role, whereas coupled photocatalysts are not formed.

The composite with a WO_3 load of 20% was the most efficient photocatalyst, extending the electrons and holes recombination time and promoting the transfer rate of electrons at the interface. The high activity of the material can be explained with its high surface area value and with the presence of WO_3 centers on the surface of TiO_2 acting as electrons/holes separators. However, if the WO_3 load is higher than 20%, a fast e^-/h^+ recombination can occur and the ability of tungsten trioxide to reduce NO_2 to NO prevails over the composites' capability to photo-oxidize NO_2 to NO_3^-. Moreover, the photodegradation activity of the heterostructures can be attributed to the oxidizing effect of holes. Moreover, it was demonstrated that high-temperature calcination leads to a partial sublimation of the WO_3 component that causes a decrease in heterostructure activity. As for the lack of the bacteria degradation, we tentatively suggest that the aggregation of nanoparticles hinders an efficient surface contact between bacteria and catalyst.

Supplementary Materials: The following supporting information can be downloaded at: https://www.mdpi.com/article/10.3390/catal12080822/s1: Table S1: EDS analysis, Figure S1: EDX spectrum of (A) WO_3@TiO_2_20* and (B) WO_3@TiO_2_20, Figure S2: Tauc plot of TiO_2 (A), WO_3@TiO_2_5 (B), WO_3@TiO_2_10 (C), WO_3@TiO_2_20 (D), WO_3@TiO_2_50 (E), WO_3@TiO_2_80 (F), WO_3 (G), Figure S3: Dependence of WO_3 content (%) in the composites versus and NO production.

Author Contributions: Conceptualization, C.L.B., F.M. and A.P.; methodology, C.L.B. and A.P.; investigation, E.F. and F.D.V.; data curation, C.L.B., F.M. and A.P.; writing—original draft preparation, E.F., F.M., C.L.B. and A.P.; writing—review and editing, E.F.; supervision, F.M.; funding acquisition, I.R.B. All authors have read and agreed to the published version of the manuscript.

Data Availability Statement: The data that support the plots within this paper are available from the corresponding author on reasonable request.

Conflicts of Interest: The authors declare no conflict of interest.

References

1. Colls, J. *Air Pollution*, 2nd ed.; CRC Press: London, UK, 2002; pp. 1–360. [CrossRef]
2. Chaloulakou, A.; Mavroidis, I.; Gavriil, I. Compliance with the annual NO_2 air quality standard in Athens. Required NO_x levels and expected health implications. *Atmos. Environ.* **2008**, *42*, 454–465. [CrossRef]
3. Roy, S.; Hegde, M.S.; Madras, G. Catalysis for NO_x abatement. *Appl. Energy* **2009**, *86*, 2283–2297. [CrossRef]
4. Ângelo, J.; Andrade, L.; Madeira, L.M.; Mendes, A. An overview of photocatalysis phenomena applied to NO_x abatement. *J. Environ. Manag.* **2013**, *129*, 522–539. [CrossRef] [PubMed]
5. Brüggemann, T.C.; Keil, F.J. Theoretical investigation of the mechanism of the selective catalytic reduction of nitric oxide with ammonia on H-form zeolites. *J. Phys. Chem. C* **2008**, *112*, 17378–17387. [CrossRef]
6. Mok, Y.S.; Lee, H. Removal of sulfur dioxide and nitrogen oxides by using ozone injection and absorption–reduction technique. *Fuel Process. Technol.* **2006**, *87*, 591–597. [CrossRef]
7. German, R.M.; Suri, P.; Park, S.J. Review: Liquid phase sintering. *J. Mater. Sci.* **2009**, *44*, 1–39. [CrossRef]
8. Zeng, Y.; Haw, K.-G.; Wang, Y.; Zhang, S.; Wang, Z.; Zhong, Q.; Kawi, S. Recent Progress of CeO_2-TiO_2 Based Catalysts for Selective Catalytic Reduction of NO_x by NH_3. *ChemCatChem* **2021**, *13*, 491–505. [CrossRef]
9. Nakata, K.; Ochiai, T.; Murakami, T.; Fujishima, A. Photoenergy conversion with TiO_2 photocatalysis: New materials and recent applications. *Electrochim. Acta* **2012**, *84*, 103–111. [CrossRef]
10. Negishi, N.; Sugasawa, M.; Miyazaki, Y.; Hirami, Y.; Koura, S. Effect of dissolved silica on photocatalytic water purification with a TiO_2 ceramic catalyst. *Water Res.* **2019**, *150*, 40–46. [CrossRef]
11. Ge, M.; Caia, J.; Iocozzi, J.; Cao, C.; Huang, J.; Zhang, X.; Shen, J.; Wang, S.; Zhang, S.; Zhang, K.-Q.; et al. A review of TiO_2 nanostructured catalysts for sustainable H_2 generation. *Int. J. Hydrog. Energy* **2017**, *42*, 8418–8449. [CrossRef]
12. Hamrouni, A.; Azzouzi, H.; Rayes, A.; Palmisano, L.; Ceccato, R.; Parrino, F. Enhanced Solar Light Photocatalytic Activity of Ag Doped TiO_2–Ag_3PO_4 Composites. *Nanomaterials* **2020**, *10*, 795. [CrossRef]
13. Braakhuis, H.M.; Gosens, I.; Heringa, M.B.; Oomen, A.G.; Vandebriel, R.J.; Groenewold, M.; Cassee, F.R. Mechanism of Action of TiO_2: Recommendations to Reduce Uncertainties Related to Carcinogenic Potential. *Annu. Rev. Pharmacol. Toxicol.* **2021**, *61*, 203–223. [CrossRef]
14. Luna, M.; Gatica, J.M.; Vidal, H.; Mosquera, M.J. One-pot synthesis of Au/N-TiO_2 photocatalysts for environmental applications: Enhancement of dyes and NO_x photodegradation. *Powder Technol.* **2019**, *355*, 793–807. [CrossRef]

15. Xu, M.; Wang, Y.; Geng, J.; Jing, D. Photodecomposition of NO$_x$ on Ag/TiO$_2$ composite catalysts in a gas phase reactor. *Chem. Eng. J.* **2017**, *307*, 181–188. [CrossRef]

16. Bianchi, C.L.; Pirola, C.; Galli, F.; Cerrato, G.; Morandi, S.; Capucci, V. Pigmentary TiO$_2$: A challenge for its use as photocatalyst in NO$_x$ air purification. *Chem. Eng. J.* **2015**, *261*, 76–82. [CrossRef]

17. Cerrato, G.; Galli, F.; Boffito, D.C.; Operti, L.; Bianchi, C.L. Correlation preparation parameters/activity for microTiO$_2$ decorated with SilverNPs for NO$_x$ photodegradation under LED light. *Appl. Catal. B Environ.* **2019**, *253*, 218–225. [CrossRef]

18. Bianchi, C.L.; Cerrato, G.; Pirola, C.; Galli, F.; Capucci, V. Photocatalytic porcelain grés large slabs digitally coated with AgNPs-TiO$_2$. *Environ. Sci. Pollut. Res.* **2019**, *26*, 36117–36123. [CrossRef]

19. Luévano-Hipólito, E.; Martínez-de la Cruz, A.; Yu, Q.L.; Brouwers, H.J.H. Precipitation synthesis of WO^3 for NO$_x$ removal using PEG as template. *Ceram. Int.* **2014**, *40*, 12123–12128. [CrossRef]

20. Yu, J.C.-C.; Lasek, J.; Nguyen, V.-H.; Yu, Y.-H.; Wu, J.C.S. Visualizing reaction pathway for the phototransformation of NO$_2$ and N$_2$ into NO over WO$_3$ photocatalyst. *Res. Chem. Intermed.* **2017**, *43*, 7159–7169. [CrossRef]

21. Kowalkińska, M.; Borzyszkowska, A.F.; Grzegórska, A.; Karczewski, J.; Głuchowski, P.; Łapiński, M.; Sawczak, M.; Zielińska-Jurek, A. Pilot-Scale Studies of WO$_3$/S-Doped g-C$_3$N$_4$ Heterojunction toward Photocatalytic NO$_x$ Removal. *Materials* **2022**, *15*, 633. [CrossRef]

22. Mendoza, J.A.; Lee, D.H.; Kang, J.-H. Photocatalytic removal of gaseous nitrogen oxides using WO$_3$/TiO$_2$ particles under visible light irradiation: Effect of surface modification. *Chemosphere* **2017**, *182*, 539–546. [CrossRef]

23. Tahir, M.B.; Nabi, G.; Rafique, M.; Khalid, N.R. Nanostructured-based WO$_3$ photocatalysts: Recent development, activity enhancement, perspectives and applications for wastewater treatment. *Int. J. Environ. Sci. Technol.* **2017**, *14*, 2519–2542. [CrossRef]

24. Wang, J.; Chen, Z.; Zhai, G.; Men, Y. Boosting photocatalytic activity of WO$_3$ nanorods with tailored surface oxygen vacancies for selective alcohol oxidations. *Appl. Surf. Sci.* **2018**, *462*, 760–771. [CrossRef]

25. Li, L.; Xiao, S.; Li, R.; Cao, Y.; Chen, Y.; Li, Z.; Li, G.; Li, H. Nanotube array-like WO$_3$ photoanode with dual-layer oxygen-evolution cocatalysts for photoelectrocatalytic overall water splitting. *ACS Appl. Energy Mater.* **2018**, *1*, 6871–6880. [CrossRef]

26. Aslam, M.; Ismail, I.M.; Chandrasekaran, S.; Hameed, A. Morphology controlled bulk synthesis of disc-shaped WO$_3$ powder and evaluation of its photocatalytic activity for the degradation of phenols. *J. Hazard. Mater.* **2014**, *276*, 120–128. [CrossRef]

27. Chu, W.; Rao, Y.F. Photocatalytic oxidation of monuron in the suspension of WO$_3$ under UV–visible light. *Chemosphere* **2012**, *86*, 1079–1086. [CrossRef]

28. Kim, D.-S.; Yang, J.-H.; Balaji, S.; Cho, H.-J.; Kim, M.-K.; Kang, D.-U.; Djaoued, Y.; Kwon, Y.-U. Hydrothermal synthesis of anatase nanocrystals with lattice and surface doping tungsten species. *CrystEngComm* **2009**, *11*, 1621. [CrossRef]

29. Riboni, F.; Bettini, L.G.; Bahnemann, D.W.; Selli, E. WO$_3$–TiO$_2$ vs. TiO$_2$ photocatalysts: Effect of the W precursor and amount on the photocatalytic activity of mixed oxides. *Catal. Today* **2013**, *209*, 28–34. [CrossRef]

30. Dozzi, M.V.; Marzorati, S.; Longhi, M.; Coduri, M.; Artiglia, L.; Selli, E. Photocatalytic activity of TiO$_2$-WO$_3$ mixed oxides in relation to electron transfer efficiency. *Appl. Catal. B Environ.* **2016**, *186*, 157–165. [CrossRef]

31. Paula, L.F.; Hofer, M.; Lacerda, V.P.B.; Bahnemann, D.W.; Patrocinio, A.O.T. Unraveling the photocatalytic properties of TiO$_2$/WO$_3$ mixed oxides. *Photochem. Photobiol. Sci.* **2019**, *18*, 2469–2483. [CrossRef]

32. Yang, L.; Si, Z.; Weng, D.; Yao, Y. Synthesis, characterization and photocatalytic activity of porousWO$_3$/TiO$_2$ hollow microspheres. *Appl. Surf. Sci.* **2014**, *313*, 470–478. [CrossRef]

33. Žerjav, G.; Arshad, M.S.; Djinović, P.; Zavašnik, J.; Pintar, A. Electron trapping energy states of TiO$_2$–WO$_3$ composites and their influence on photocatalytic degradation of bisphenol. *Appl. Catal. B Environ.* **2017**, *209*, 273–284. [CrossRef]

34. Shifu, C.; Lei, C.; Shen, G.; Gengyu, C. The preparation of coupled WO$_3$/TiO$_2$ photocatalyst by ball milling. *Powder Technol.* **2005**, *160*, 198–202. [CrossRef]

35. Makwana, N.M.; Hazael, R.; McMillan, P.F.; Darr, J.A. Photocatalytic water disinfection by simple and low-cost monolithic and heterojunction ceramic wafers. *Photochem. Photobiol. Sci.* **2015**, *14*, 1190–1196. [CrossRef] [PubMed]

36. Dhanalekshmi, K.I.M.; Umapathy, J.; Magesan, P.; Zhang, X. Biomaterial (Garlic and Chitosan)-Doped WO$_3$-TiO$_2$ Hybrid Nanocomposites: Their Solar Light Photocatalytic and Antibacterial Activities. *ACS Omega* **2020**, *5*, 31673–31683. [CrossRef] [PubMed]

37. Manmohan, L.; Praveen, S.; Chhotu, R. Calcination temperature effect on titanium oxide (TiO$_2$) nanoparticles synthesis. *Optik* **2021**, *241*, 166934. [CrossRef]

38. El-Yazeed, W.S.A.; Ahmed, A.I. Photocatalytic activity of mesoporous WO$_3$/TiO$_2$ nanocomposites for the photodegradation of methylene blue. *Inorg. Chem. Commun.* **2019**, *105*, 102–111. [CrossRef]

39. Boruah, P.J.; Khanikar, R.R.; Bailung, H. Synthesis and Characterization of Oxygen Vacancy Induced Narrow Bandgap Tungsten Oxide (WO$_{3-x}$) Nanoparticles by Plasma Discharge in Liquid and Its Photocatalytic Activity. *Plasma Chem. Plasma Process* **2020**, *40*, 1019–1036. [CrossRef]

40. Kathiravan, A.; Renganathan, R. Photosensitization of colloidal TiO$_2$ nanoparticles with phycocyanin pigment. *J. Colloid Interface Sci.* **2009**, *335*, 196–202. [CrossRef]

41. Gutiérrez-Alejandre, A.; Castillo, P.; Ramírez, J.; Ramis, G.; Busca, G. Redox and acid reactivity of wolframyl centers on oxide carriers: Brønsted, Lewis and redox sites. *Appl. Catal. A* **2001**, *216*, 181–194. [CrossRef]

42. Lv, K.; Li, J.; Qing, X.; Li, W.; Chen, Q. Synthesis and photodegradation application of WO$_3$/TiO$_2$ hollow spheres. *J. Hazard. Mater.* **2011**, *189*, 329–335. [CrossRef]

43. Nguyen, T.T.; Nam, S.N.; Son, J.; Oh, J. Tungsten Trioxide (WO$_3$)-assisted Photocatalytic Degradation of Amoxicillin by Simulated Solar Irradiation. *Sci. Rep.* **2019**, *9*, 9349. [CrossRef]

44. Dirany, N.; Arab, M.; Madigou, V.; Leroux, C.; Gavarri, J.R. A facile one step route to synthesize WO$_3$ nanoplatelets for CO oxidation and photodegradation of RhB: Microstructural, optical and electrical studies. *RSC Adv.* **2016**, *6*, 6961–69626. [CrossRef]

45. Lasek, J.; Yu, Y.-H.; Wu, Y.C.S. Removal of NO$_x$ by photocatalytic processes. *J. Photochem. Photobiol. C Photochem. Rev.* **2013**, *14*, 29–52. [CrossRef]

46. Dalton, J.S.; Janes, P.A.; Jones, N.G.; Nicholson, J.A.; Hallam, K.R.; Alle, G.C. Photocatalytic oxidation of NO$_x$ gases using TiO$_2$: A surface spectroscopic approach. *Environ. Pollut.* **2002**, *120*, 415–422. [CrossRef]

47. Wu, J.C.S.; Cheng, Y.-T. In situ FTIR study of photocatalytic NO reaction on photocatalysts under UV irradiation. *J. Catal.* **2006**, *237*, 393–404. [CrossRef]

48. Balayeva, N.O.; Fleisch, M.; Bahnemann, D.W. Surface-grafted WO$_3$/TiO$_2$ photocatalysts: Enhanced visible-light activity towards indoor air purification. *Catal. Today* **2018**, *313*, 63–71. [CrossRef]

49. Rampaul, A.; Parkin, I.P.; O'Neill, S.A.; DeSouza, J.; Mills, A.; Elliott, N. Titania and tungsten doped titania thin films on glass; active photocatalysts. *Polyhedron* **2003**, *22*, 35–44. [CrossRef]

50. Wang, W.; Zeng, Z.; Zeng, G.; Zhang, C.; Xiao, R.; Zhou, C.; Xiong, W.; Yang, Y.; Lei, L.; Liu, Y.; et al. Sulfur doped carbon quantum dots loaded hollow tubular g-C$_3$N$_4$ as novel photocatalyst for destruction of *Escherichia coli* and tetracycline degradation under visible light. *Chem. Eng. J.* **2019**, *378*, 122132. [CrossRef]

51. Yang, Y.A.; Ma, Y.; Yao, J.N.; Loo, B.H. Simulation of the sublimation process in the preparation of photochromic WO$_3$ film by laser microprobe mass spectrometry. *J. Non-Cryst. Solids* **2000**, *272*, 71–74. [CrossRef]

52. Blattner, F.R.; Plunkett, G.; Bloch, C.A.; Perna, N.T.; Burland, V.; Riley, M.; Collado-Vides, J.; Glasner, J.D.; Rode, C.K.; Shao, Y. The complete genome sequence of *Escherichia coli* K-12. *Science* **1997**, *277*, 1453–1462. [CrossRef] [PubMed]